Invited Paper

Computer modeling of laser melting and spallation of metal targets

Leonid V. Zhigilei*, Dmitriy S. Ivanov, and Elodie Leveugle

Department of Materials Science and Engineering, University of Virginia
116 Engineer's Way, Charlottesville, Virginia 22904-4745

Babak Sadigh and Eduardo M. Bringa

Lawrence Livermore National Laboratory, Livermore, California 94551

ABSTRACT

The mechanisms of melting and photomechanical damage/spallation occurring under extreme superheating/deformation rate conditions realized in short pulse laser processing are investigated in a computational study performed with a hybrid atomistic-continuum model. The model combines classical molecular dynamics method for simulation of non-equilibrium processes of lattice superheating and fast phase transformations with a continuum description of the laser excitation and subsequent relaxation of the conduction band electrons. The kinetics and microscopic mechanisms of melting are investigated in simulations of laser interaction with free-standing Ni films and bulk targets. A significant reduction of the overheating required for the initiation of homogeneous melting is observed and attributed to the relaxation of laser-induced stresses, which leads to the uniaxial expansion and associated anisotropic lattice distortions. The evolution of photomechanical damage is investigated in a large-scale simulation of laser spallation of a 100 nm Ni film. The evolution of photomechanical damage is observed to take place in two stages, the initial stage of void nucleation and growth, when both the number of voids and the range of void sizes are increasing, followed by the void coarsening, coalescence and percolation, when large voids grow at the expense of the decreasing population of small voids. In both regimes the size distributions of voids are found to be well described by the power law with an exponent gradually increasing with time. A good agreement of the results obtained for the evolution of photomechanical damage in a metal film with earlier results reported for laser spallation of molecular systems and shock-induced back spallation in metals suggests that the observed processes of void nucleation, growth and coalescence may reflect general characteristics of the dynamic fracture at high deformation rates.

Keywords: laser melting, laser spallation, dynamic fracture, molecular dynamics, computer modeling

1. INTRODUCTION

Short (pico- and femtosecond) pulse laser irradiation has the ability to bring material into a highly non-equilibrium state and provides unique opportunity to study the material behavior under extreme conditions that can hardly be achieved by any other means. Analysis of the laser-induced processes leads to a range of important fundamental questions, such as the limit of superheating and the microscopic mechanisms of homogeneous and heterogeneous melting, the nature of the fracture/spallation at ultra-high deformation rates and elevated temperatures, as well as the mechanisms of explosive boiling and disintegration of material in laser ablation. Recent progress in the development of new optical and x-ray, and electron diffraction time-resolved probe techniques has provided valuable information on the time-scales of ultrafast phase transformations, e.g. [1,2,3,4,5,6]. A reliable interpretation of experimental observations requires a better understanding of the microscopic mechanisms and kinetic limits of the processes responsible for the phase transformations and fracture occurring under the extreme conditions created in the target material by short pulse laser irradiation.

In this paper we present the results of atomic-level simulations of short pulse laser melting and spallation of metal targets. A hybrid computational model that combines classical molecular dynamics (MD) method for simulation

* lz2n@virginia.edu; Phone: (434) 243 3582; Fax: (434) 982 5660; http://www.faculty.virginia.edu/CompMat/

In *High-Power Laser Ablation V*, Claude R. Phipps, Editor
Proceedings of SPIE, Vol. 5448 (2004)

of non-equilibrium processes of lattice superheating, fast phase transformations and fracture with a continuum description of the laser excitation and subsequent relaxation of the conduction band electrons based on the two-temperature model (TTM), is used in the simulations. First applications of the TTM-MD model have already provided insights into the microscopic mechanisms of laser melting and disintegration of Ni and Au films [7,8,9], photomechanical spallation of bulk Ni targets [10], as well as disintegration and ablation of Cu targets [11]. The hybrid TTM-MD model was also used in a recent study of shock-induced heating and melting of a grain boundary region in an Al crystal [12]. A brief description of the TTM-MD model as well as the parameters of the model used in the simulations presented in this paper are given below, in Section 2. The results of the simulations of laser melting of Ni targets are presented and related to the results obtained for homogeneous melting occurring under controlled temperature/stress conditions in Section 3. Computational analysis of the void nucleation, growth and coalescence in photomechanical spallation is presented in Section 4.

2. COMPUTATIONAL MODEL

In metals, laser light is absorbed by the conduction band electrons. The deposited energy quickly, within femtoseconds, is equilibrated among the electrons and, more slowly, is transferred to the lattice vibrations. The later process is controlled by the strength of the electron-phonon coupling and can take from fractions of a picosecond to several tens of picoseconds. Finally, a thermal equilibrium is established between the electrons and phonons, and the common thermal diffusion can be used to describe the heat flow into the bulk of the irradiated target. In this section we first briefly present a computational model that we are developing for simulations of laser interaction with metals and then describe the model systems used for investigation of the mechanisms of laser melting and spallation.

2.1. Combined atomistic - continuum model for simulation of laser interaction with metal targets

Several modifications have to be made in order to apply the classical MD method for simulation of laser interactions with metals. Since the electronic contribution to the thermal conductivity of a metal is dominant, the conventional MD method, where only lattice contributions are present, significantly underestimates the total thermal conductivity. This leads to unphysical confinement of the deposited laser energy in the surface region of the irradiated target and does not allow for the direct comparison between the calculated and experimental data. Straightforward application of the Fourier's law or the equation of heat conduction in metals [13] implies that a complete local thermal equilibrium is reached between the electrons and phonons. This assumption is correct as soon as the duration of the laser pulse is much longer than the characteristic time of electron-phonon relaxation. For ps- and fs-pulses, however, the electron-phonon equilibrium cannot be assumed *a priori* and the time evolution of the lattice and electron temperatures, T_l and T_e, is typically described within a so-called two-temperature model (TTM) [14,15], by two coupled non-linear differential equations. Over the last decades, TTM has become the main model to describe the kinetics of the electron and lattice temperature evolution in a target irradiated with a short laser pulse, e.g. [5,16,17,18,19,20,21]. Despite the successful applications and popularity of TTM, however, the inherent limitation of the model is its inability to adequately describe the kinetics of phase transformations occurring under highly nonequilibrium conditions induced in the target material by short pulse laser irradiation. Moreover, TTM does not account for thermoelastic stresses that can be induced by fast laser energy deposition and thermoelasticity equations should be added to account for the possibility of nonthermal damage to the target [22].

In order to overcome these limitations we are developing a hybrid computational model that combines classical MD method for simulation of non-equilibrium processes of lattice superheating and fast phase transformations with a continuum description of the laser excitation and subsequent relaxation of the conduction band electrons, based on TTM. In the combined TTM-MD method, schematically illustrated in Figure 1, MD substitutes the TTM equation for the lattice temperature. The diffusion equation for the electron temperature, T_e, is solved by a finite difference method simultaneously with MD integration of the equations of motion of atoms. The electron temperature enters a coupling term that is added to the MD equations of motion to account for the energy exchange between the electrons and the lattice [8]. The time steps in the two parts of the combined model are chosen so that one MD time step would correspond to an integer number of time steps of finite difference integration of the TTM equation for the electronic temperature, $\Delta t_{MD} = n\Delta t_{FD}$. In each finite difference discretization cell, the energy transferred between the electrons and the lattice due to the electron-phonon coupling is accumulated for n steps of integration and then transferred to the corresponding part of the MD system by means of the coupling term.

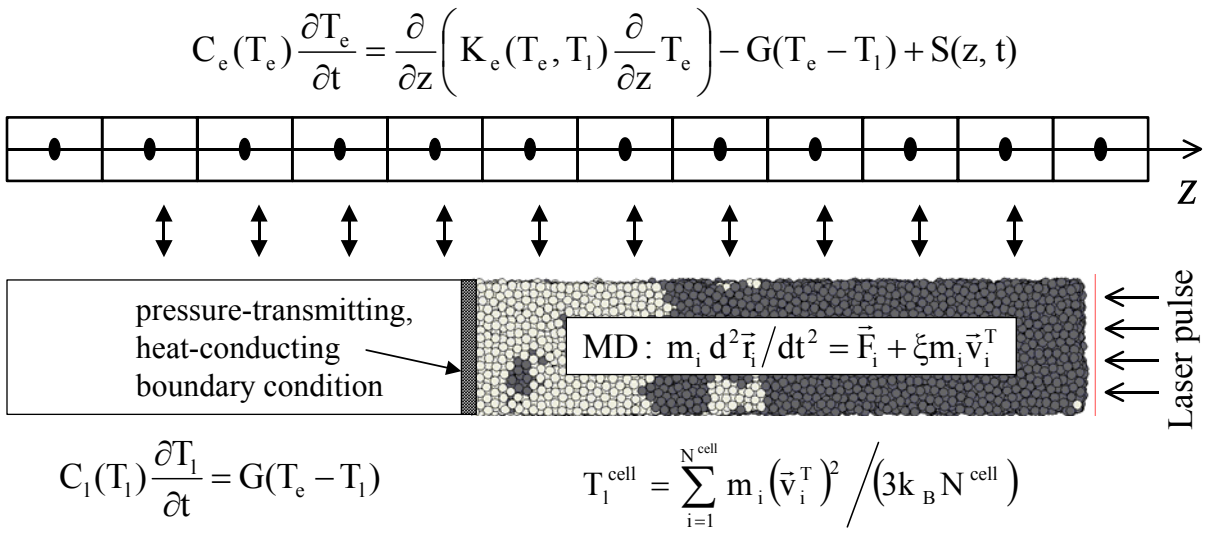

Figure 1. Schematic representation of the combined continuum-atomistic model for simulation of laser interaction with a metal target. The evolution of electron temperature is described by a non-linear differential equation, whereas the atomic motions are described by the MD method with an additional term, $\xi m_i \vec{v}_i^{\,T}$, added to the ordinary MD equations of motion to account for the electron-phonon coupling. Spatial discretization in the continuum model (typically ~1 nm) and size of the atomistic region are not drawn to scale. The cells in the finite difference discretization are related to the corresponding volumes of the MD system and the local lattice temperature, T_l^{cell}, is defined for each cell from the average kinetic energy of thermal motion of atoms. Thermal velocity of an atom is defined as $\vec{v}_i^{\,T} = \vec{v}_i - \vec{v}^{\,c}$, where $\vec{v}_i$ is the actual velocity of an atom i, and $\vec{v}^{\,c}$ is the velocity of the center of mass of a cell to which atom i belongs. A Gaussian temporal profile, S(z,t), is used to describe the laser excitation of the conduction band electrons. The expansion, density variations and, at higher fluences, disintegration of the irradiated target predicted in the MD part of the model are accounted for in the continuum part of the model. A complete description of the combined TTM-MD model is given in [8].

The MD method is used only in the very surface region of the target, where active processes of laser melting and ablation are taking place, whereas the diffusion equation for the electron temperature is solved in a much wider region affected by the thermal conduction. A special pressure-transmitting boundary condition [23,24] is used to imitate the propagation of the laser-induced pressure wave from the MD region of the computational cell to the continuum part of the model. The energy carried away by the wave is monitored, allowing for control over the energy conservation in the combined model. Periodic boundary conditions are imposed in the directions parallel to the surface. These conditions simulate the situation in which the laser spot diameter is large compared to the depth of the laser energy deposition, so that the effects of the edges of the laser beam can be neglected. In the part of the computational cell beyond the MD region (left part in Figure 1), the energy exchange between the electrons and the lattice is described by a conventional TTM, in which the phonon contribution to the heat conduction is neglected. The temperature dependence of the lattice heat capacity, $C_l(T_l)$, obtained for the model material is approximated by a polynomial function and used in the TTM equation for the lattice temperature.

The hybrid atomistic-continuum model, briefly described above, combines the advantages of TTM and MD methods. TTM provides an adequate description of the laser energy deposition into the electronic system, energy exchange between the electrons and phonons, and fast electron heat conduction in metals, whereas the MD method is appropriate for simulation of rapid non-equilibrium phase transformations, damage and ablation. In this paper we apply the model for investigation of the mechanisms of laser melting and spallation of Ni targets. Computational setup and parameters of the model systems used in the simulations are described below.

2.2. Computational setup and parameters of the model

Simulations reported in this paper are done for nickel, a transition metal with strong electron-phonon coupling and a relatively small, as compared to other metals, thermal diffusivity. The strong electron-phonon coupling in Ni leads to a rapid transfer of the absorbed energy to the lattice and confines the initial laser energy deposition in a shallow surface region of the irradiated target. The energy confinement allows for a realistic simulation of laser interaction with a bulk target with a MD computational cell of only 100 nm in depth, as demonstrated in Section 3.1. Inter-atomic interaction in the MD part of the model is described by the embedded-atom method (EAM) [25], which provides a computationally efficient but rather realistic description of bonding in metals and allows for simulation of sufficiently large systems. A functional form and parameterization of the EAM potential suggested in Ref. [26] is used in this work.

The choice of the inter-atomic potential defines all the thermal and elastic properties of the lattice, such as the lattice heat capacity, elastic moduli, the coefficient of thermal expansion, melting temperature, volume and entropy of melting and vaporization, as well as the dependence of these characteristics on temperature and pressure. In order to provide an adequate interpretation of the simulation results the parameters of the model material should be first determined. A series of liquid-crystal coexistence simulations are performed to find the pressure dependence of the equilibrium melting temperature. Constant-temperature-constant-pressure simulations were used to determine the temperature and pressure dependence of volume, internal energy, heat capacity, and coefficient of thermal expansion for both liquid and solid phases of the EAM Ni material. Some of the properties relevant to the melting process are listed in Table 1, along with experimental data for Ni. While there are some quantitative discrepancies between the properties of the model EAM Ni and experimental data, the overall agreement is reasonable and we can expect that the model will adequately reproduce the material response to fast laser heating. Moreover, the knowledge of thermodynamic parameters of the model material will allow us to perform a quantitative analysis and physical interpretation of the simulation results.

Properties	T_m, K	ΔV_m, $cm^3\ mol^{-1}$	ΔS_m, $J\ K^{-1}\ mol^{-1}$	ΔH_m, $kJ\ mol^{-1}$	$(dT/dP)_m$, $K\ GPa^{-1}$	$(dT/dP)_S$, $K\ GPa^{-1}$	C_p, $J\ K^{-1}\ mol^{-1}$	α, $10^6\ K^{-1}$
EAM Ni	1439	0.46	10.06	14.47	45.79	30.4	25.04 - 36.13	14.4 - 22.6
Experiment	1726	0.45	9.94	17.47	45.27	24.8	25.85 - 46.50	12.8 - 17.5

Table 1. Some of the material parameters determined for the EAM Ni material. Values of the equilibrium melting temperature, T_m, volume change, ΔV_m, enthalpy, ΔH_m, and entropy, ΔS_m, of melting are given for zero pressure. The dependence of the equilibrium melting temperature on pressure, $(dT/dP)_m$, is determined from the liquid-crystal coexistence simulations performed at different pressures and confirmed by the calculations based on the Clapeyron equation, $(dT/dP)_m=\Delta V_m/\Delta S_m$. We find that both ΔV_m and ΔS_m decrease with increasing pressure, leading to a weak pressure dependence of $(dT/dP)_m$, it changes from 42.4 K/GPa to 46.8 K/GPa within the pressure range from -5 GPa to 12 GPa. The value given in the table is calculated for zero pressure. The temperature variation with pressure for an isentropic expansion/compression, $(dT/dP)_S$, is calculated as discussed in Refs. [7,8] and is given for the crystal phase at T_m and zero pressure. Variations of the coefficient of linear expansion, α, and heat capacity at zero pressure, C_p, are given for a temperature range from 293 K to 1000 K. Experimental values for Ni are calculated based on data given in Refs. [27,28].

The parameters used in the continuum part of the model (TTM equation for the electron temperature) are listed in Table 2. A simple linear dependence of the electron thermal conductivity on the electron temperature, $K_e = K_0 T_e/T_l$, is used in the calculations. For a range of laser fluences used in this work, justification of this approximation, which neglects the effect of the electron-electron scattering, is given in Ref. [8]. The mean free path of electrons in Ni is of the same order as the optical penetration depth and ballistic energy transport is not taken into account in the simulations.

A, $J\ m^{-3}\ K^{-2}$	K_0, $W\ m^{-1}\ K^{-1}$	G, $W\ m^{-3}\ K^{-1}$	L_p, nm
1065	91	3.6×10^{17}	13.5

Table 2. Parameters used in the TTM equation for the electron temperature. The parameters used in the expressions for the electronic heat capacity, $C_e = AT_e$, and thermal conductivity, $K_e = K_0 T_e/T_l$, as well as the electron-phonon coupling constant, G, and the optical absorption depth, L_p are from Ref. [5].

Simulations of laser melting reported in this paper are performed for a free-standing 50 nm Ni film and for a bulk Ni target. The initial MD computational cell used in representation of the 50 nm film is an FCC crystal with lateral dimensions of 3.53×3.53 nm. The number of atoms in the computational cell is 56800 atoms. Simulations of laser interaction with bulk targets are performed for two sizes of the MD part of the combined TTM-MD model, $1.77 \times 1.77 \times 99.94$ nm (28300 atoms) and $7.06 \times 3.53 \times 99.94$ nm (226400 atoms). The continuum part of the combined TTM-MD model extends by 500 nm beyond the back end of the MD computational cell, Figure 1, providing an adequate representation of the electronic heat conduction into the bulk of the target. Periodic boundary conditions are applied in the lateral directions, parallel to (100) free surface(s). Before applying laser irradiation, all systems are equilibrated at 300 K. The absorbed laser fluence, rather then the incident fluence, is used in the discussion of the simulation results.

By comparing the results of the simulations of laser spallation obtained for systems with different sizes in the lateral (parallel to the surface) directions we find that while the general mechanisms of film damage and disintegration are not affected by the lateral sizes of the MD cell, the threshold fluences for disintegration/spallation are lower for smaller computational cells due to the effect of the periodic boundary conditions. Moreover, a reliable quantitative analysis of the microscopic mechanisms of the photomechanical damage and spallation (e.g. evolution of the void size distribution) can be only performed for sufficiently large systems, where the largest void is still significantly smaller than the size of the computational cell. Therefore, in order perform a quantitative analysis of spallation mechanisms we performed an additional larger scale simulation for a 100 nm Ni film with lateral dimensions of the computational cell of 17.6×17.6 nm (2,800,000 atoms). A three-dimensional solution of the TTM equation for the electron temperature is used in this simulation to account for possible generation of the electron temperature gradients in the lateral directions during the spallation process.

3. LASER MELTING

Experimental investigations of the ultrafast phase transformations in metals and semiconductors [1,2,3,4,5,6] performed by various time-resolved pump-probe techniques suggest that, depending on the irradiation conditions and properties of the material, the melting of the surface layer can take from several picoseconds to nanoseconds. The melting time of several hundreds of picoseconds and longer [4,6] is consistent with a conventional picture of heterogeneous nucleation of the liquid phase at the irradiated surface and propagation of the melting front deeper into the bulk of the crystal [29]. A typical thickness of the layer affected by the ultrashort laser heating is on the order of 100 nm for metals or semiconductors, whereas the velocity of the melting front propagation has a strong dependence on the degree of superheating, but is ultimately limited by the speed of sound [30]. The melting time of several picoseconds [1,2,3] is too short to be explained by the heterogeneous melting mechanism, and the melting can be attributed to homogeneous nucleation of the liquid phase inside the superheated surface region. Therefore, depending on the irradiation condition, optical and thermal properties of the material, and the time of the electron-phonon equilibration in the system, the dynamics of laser melting is defined by either or both propagation of the melting front from the surface and homogeneous nucleation of the liquid phase in the bulk of the superheated crystal, as schematically shown in Figure 2.

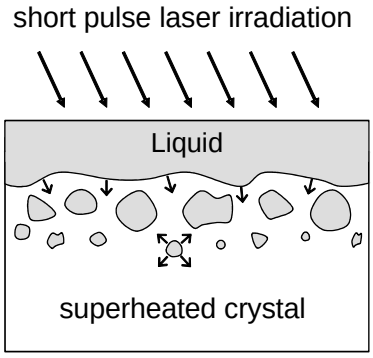

Figure 2. Schematic sketch of the short pulse laser melting process: competition between the melting front propagation from the surface and homogeneous nucleation of the liquid phase.

At the extremely high levels of overheating and short times of phase transformations, direct applicability of macroscopic kinetic approaches based on classical nucleation theory to short pulse laser melting [29,30,31,32] is questionable and should be verified by a detailed atomic-level analysis of the involved processes. In this section we report the results of computational investigation of the mechanisms and kinetics of laser melting of a thin Ni film and a bulk Ni target and relate our observations to the results of the simulations of homogeneous melting performed under well-controlled pressure and temperature conditions.

3.1. Laser melting: interplay of homogeneous and heterogeneous melting mechanisms

The mechanisms of laser melting are discussed in this section based on the results of two MD simulations of laser irradiation of 50 nm free-standing Ni film and a bulk Ni target. The same absorbed laser fluence of 430 J/m^2 is used in both simulations. The lattice temperature contour plots are shown in Figures 3a and 3c. Laser energy is deposited during the laser pulse to the conduction band electrons and the energy transfer from hot electrons to the lattice leads to the initial temperature increase during the first 10-15 ps. Strong electron-phonon coupling in Ni results in the development of lattice temperature gradient in both the 50 nm film and the bulk target. By the time of ~10 ps the temperature in the surface layers of the irradiated targets increases up to ~1650 K, significantly above the equilibrium

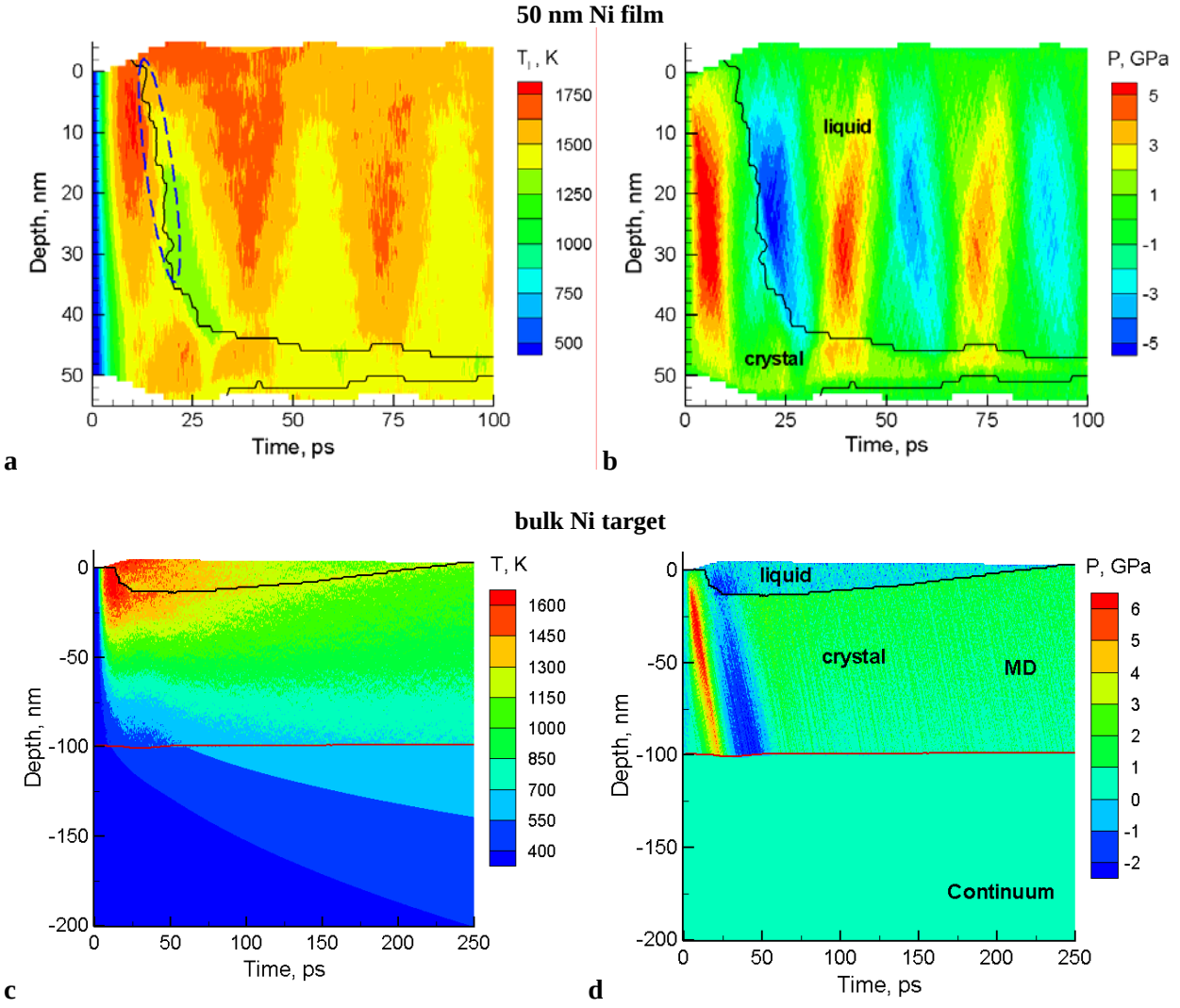

Figure 3. Temperature (a, c) and pressure (b, d) contour plots for simulations of laser melting of a 50 nm Ni film irradiated with a 200 fs laser pulse (a, b) and a bulk Ni target irradiated with a 1 ps laser pulse (c, d). The same absorbed fluence of 430 J/m^2 is used in both simulations. Laser pulse is directed along the Y-axes, from the top of the contour plots. Black lines separate the melted regions from the crystalline parts of the targets. Red lines in (c) and (d) separate the MD and continuum parts of the combined TTM-MD model (see Figure 1). Pressure is not calculated in the continuum part of the current version of the model, but the energy of the pressure wave in the continuum part of the model is accounted for. Blue dashed line in (a) marks the region of the contour plot where homogeneous melting takes place in the 50 nm film. The temperature/pressure conditions in this region are shown in Figure 5 by color circles.

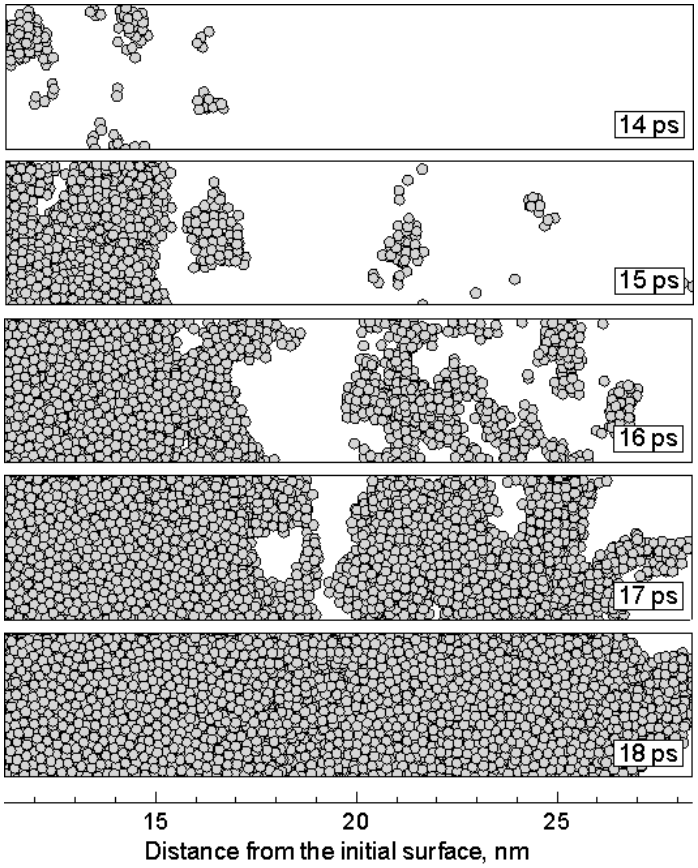

Figure 4. Homogeneous melting process as seen in snapshots from simulation of a 50 nm Ni film irradiated with a 200 fs laser pulse at an absorbed fluence of 430 J/m^2. Snapshots are taken at times and locations when/where homogeneous melting is observed in the simulation (area marked by a blue dashed line in Figure 3a). Only atoms that belong to the liquid phase are shown in the snapshots. The crystal and liquid phases are distinguished based on the local order parameter defined in [8].

melting temperature of 1439 K, determined for the EAM Ni from a liquid-crystal coexistence simulation at zero pressure. During the following 10-15 ps we observe an ultrafast melting of a large fraction (~35 nm) of the 50 nm film and ~15 nm layer of the bulk target. The melted parts of the targets are separated from the crystalline parts by black lines in Figure 3.

Although, at first sight, the melting seems to proceed by propagation of the melting front from the irradiated surface, a closer look at a series of snapshots of the atomic-level structure of a region undergoing ultrafast melting, Figure 4 and [33], reveals a more complex picture characteristic of homogeneous melting. Small liquid regions appear and grow ahead of the "melting front" leading to a very high apparent "melting front" propagation velocity significantly exceeding the speed of sound. Even faster thermal melting of the overheated material was observed at higher fluences, when a collapse of the crystal structure overheated above the limit of crystal stability takes place simultaneously in a large region within several picoseconds [8]. This time, comparable to several periods of atomic vibrations, can be considered to be the minimum time required for the thermal melting. It is in a good agreement with the results of recent ultrafast time-resolved electron diffraction experiments [1], where a solid-liquid phase transition in a 20 nm aluminum film was observed to be completed within 3.5 ps following irradiation by a 120 fs 700 J/m^2 laser pulse.

3.2. Laser melting: the effect of pressure relaxation and uniaxial expansion

While the initial ultrafast homogeneous melting of overheated surface regions takes place in both the 50 nm film and the bulk target, further evolution of temperature and pressure, as well as the evolution of the melted regions is very different. In the 50 nm film the deposited laser energy is trapped in the film and the lattice temperature gradually evolves towards the even distribution throughout the film. The temperature evolution is strongly affected by the relaxation of the laser-induced pressure. The initial high compressive stresses created in the irradiated free-standing film under conditions of stress confinement [8,10] lead to the expansion of the film with tensile stresses concentrating in the central part of the film. The following gradually dissipating oscillations of the film continue beyond the time of the

simulation, Figure 3b. A direct correlation between the pressure and temperature variations in the film is apparent from comparison of Figures 3a and 3b. Compression leads to the temperature increase whereas expansion corresponds to cooling. Quantitative thermodynamic analysis performed in Refs. [7,8] confirms that the temperature variation with pressure can be attributed to the adiabatic/isentropic expansion of the film. It has been also shown in [8,9] that the non-thermal energy of elastic oscillations of the film can account for a significant (up to ~15%) of the total energy deposited by the laser pulse. A gradual dissipation of the oscillations, occurring on the timescale of picoseconds, leads to the energy transfer from the energy of the elastic vibrations to the energy of the thermal motion of the atoms. In the simulations performed at laser fluences close to the melting threshold this energy transfer resulted in a gradual advancement of the melting fronts in long-term heterogeneous melting of the film [9]. In the simulation illustrated in Figures 3a and 3b, a complete melting of the film is observed, with the crystalline region near the back surface of the film vanishing by the time of ~115 ps after the laser pulse.

In the case of laser melting of a bulk target, Figures 3c and 3d, there is no reflection of the compressive and tensile components of the laser-induced pressure wave, which propagates through the non-reflecting boundary at the bottom of the MD part of the combined atomistic-continuum model. The evolution of the temperature in the bulk target is mainly defined by the fast electronic heat conduction to the bulk of the target, which leads to the fast cooling and recrystallization of the melted region. The recrystallization process is completed by the time of 250 ps.

An abrupt change in the pressure values upon crossing the crystal-liquid interface in Figure 3d is related to the confinement of the heated crystalline material in the lateral directions [10]. For a typical laser spot diameter of ~100 μm, the fast relaxation of the laser-induced pressure can only proceed in the direction normal to the surface. These conditions of lateral confinement are correctly reproduced by the periodic boundary conditions used in the directions parallel to the surface. In the melted part of the target the stresses remain isotropic during the uniaxial expansion of the surface region and the pressure is defined only by the volume and temperature. The uniaxial expansion of the crystalline part of the target, however, results in anisotropic lattice deformations and corresponding anisotropic stresses. The anisotropic stresses in a crystal cannot relax by uniaxial expansion and the residual compressive stresses remain in the crystalline part of the target long after the relaxation of the transient thermoelastic stresses in the melted part.

The dynamics of the relaxation of the laser-induced stresses not only affects the temperature evolution, but also have a direct impact on the conditions leading to the homogeneous laser melting discussed above, in Section 3.1 and illustrated in Figure 4. The temperature and pressure conditions leading to the onset of the homogeneous laser melting are shown in Figure 5 by color circles. At all pressures, the homogeneous melting starts under conditions of overheating above the liquid-crystal coexistence line. The overheating required for initiation of the homogeneous melting, however, is found to range from less than 1.05 T_m to 1.18 T_m. These values are significantly lower then the temperatures at which homogeneous melting is observed in constant hydrostatic pressure simulations performed with three-dimensional periodic boundary conditions, 1.21 - 1.25 T_m, shown by red squares connected by the black dashed line in Figure 5.

The discrepancy between the maximum overheating under constant pressure conditions and the one required for the initiation of homogeneous melting under the short pulse laser irradiation conditions can be explained by the dynamics of the relaxation of the laser-induced pressure. As briefly discussed above, the relaxation of the laser-induced pressure can only proceed in the direction normal to the surface. This uniaxial expansion and associated anisotropic lattice distortions can additionally reduce the lattice stability against the initiation of melting. In order to test this hypothesis, we performed a series of constant-pressure simulations under conditions of uniaxial expansion, when the sizes of the computational cell in the lateral directions were fixed at values that correspond to zero pressure at a temperature of 300 K and relaxation is only allowed in one direction. These simulations predict the temperature and pressure conditions for the onset of homogeneous melting (green diamonds in Figure 5) that fit well with the conditions realized in the simulation of laser melting (color circles in Figure 5). Note, that under conditions of uniaxial expansion the value of pressure, defined as negative one third of the first invariant of the stress tensor, $P = -(\sigma_{xx} + \sigma_{yy} + \sigma_{zz})/3$, contains different contributions from different diagonal components of the stress tensor. For example, for melting conditions at zero pressure the lattice parameter in lateral (x and y) directions is fixed at $a_0 = 0.353$ nm, lattice parameter in z direction is $a_1 = 0.394$ nm, and stresses are $\sigma_{xx} = \sigma_{yy} = -0.66$ GPa, and $\sigma_{zz} = 1.32$ GPa.

The melting process under conditions of short pulse laser irradiation proceeds simultaneously with the uniaxial expansion of the film, Figure 3b, leading to the decrease of pressure and the corresponding decrease of the overheating needed for the initiation of the homogeneous melting. This is apparent from Figure 5, where the points corresponding

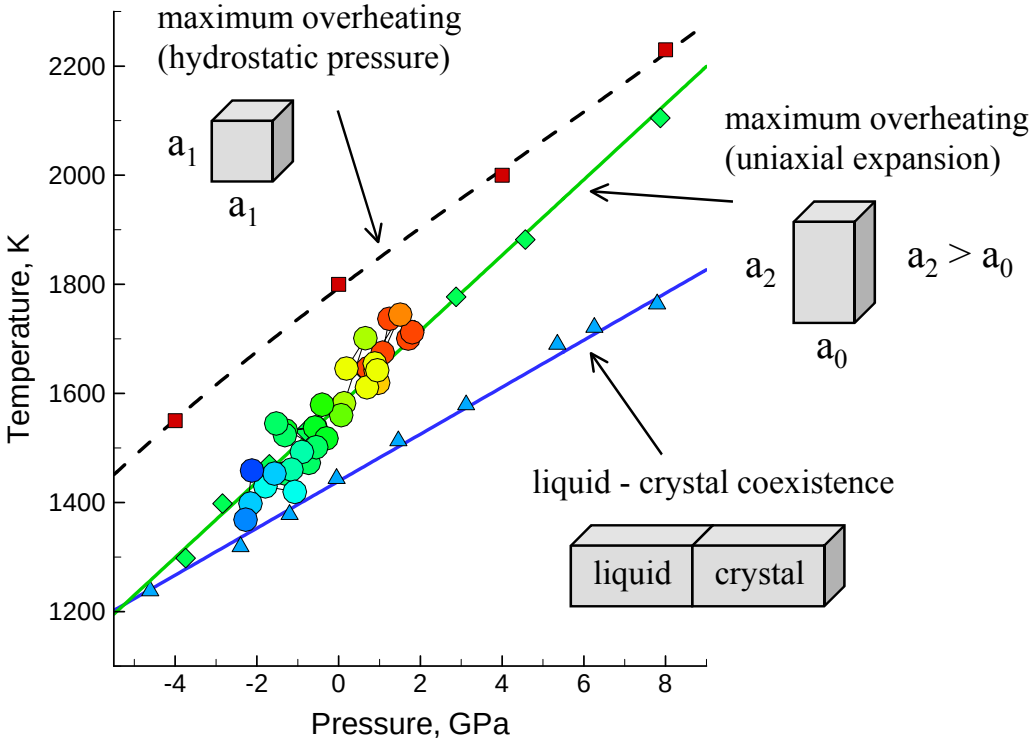

Figure 5. Pressure/temperature conditions for equilibrium and non-equilibrium melting observed in simulations performed for EAM Ni material. Blue triangles correspond to the conditions of equilibrium melting obtained in liquid-crystal coexistence simulations. Red squares connected by the black dashed line correspond to the maximum overheating of a crystal observed in simulations performed with 3D periodic boundary conditions and constant hydrostatic pressure. Green diamonds show the conditions for homogeneous melting in simulations of uniaxial expansion. Color circles show to the conditions leading to the onset of homogeneous melting in the simulation of laser melting illustrated in Figures 3a,b and 4. The time and location of the homogeneous melting are marked in Figure 3a by a blue dashed line. The circles are connected by lines and colored from red to blue in the order of increasing depth under the surface.

to the onset of the homogeneous melting are approaching the coexistence line as depth (and time) increases. As a result, our simulations suggest that homogeneous melting can be induced at significantly lower values of overheating and larger range of irradiation parameters as compared to the predictions based on the classical nucleation theory [31].

4. LASER SPALLATION

The relaxation of laser-induced stresses not only affects the kinetics and mechanisms of laser melting (see Section 3.2) but, at higher laser fluences, can lead to cavitation and disruption of a liquid/melted surface region of the irradiated target or mechanical fracture/spallation of a solid target. The maximum values of the laser-induced stresses and the contribution of photomechanical effects to the onset of laser damage and spallation are related to the condition of the stress confinement [10,34,35]. In systems with relatively slow heat conduction and fast thermalization of the deposited laser energy, the condition for stress confinement is mainly defined by the laser penetration depth, L_p and the laser pulse duration, τ_p. It can be written as $\tau_p \leq \tau_s \sim L_p/C_s$, where C_s is the speed of sound in the target material. In metals, the strength of the electron-phonon coupling and much faster electron heat conduction are additional factors that affect the maximum thermoelastic pressure that can be created in the target. The characteristic time of the energy transfer from the excited hot electrons to the lattice, $\tau_{e\text{-}ph}$, and the diffusive/ballistic penetration depth of the excited

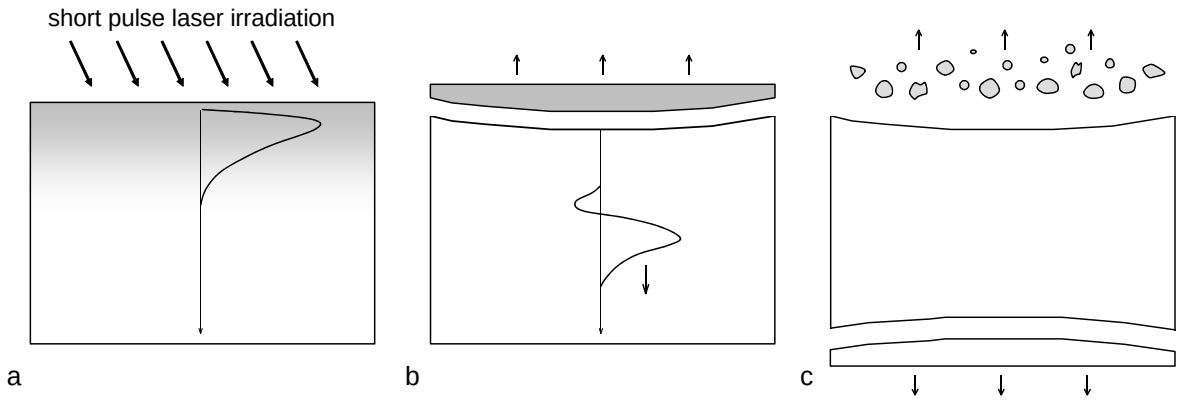

Figure 6. Schematic representation of the processes involved in laser-induced front and back surface spallation: (a) generation of high compressive stresses in the surface region of the irradiated target; (b) propagation of the pressure wave deeper into the target, development of the tensile component of the pressure wave, separation and ejection of a front layer of the target (front-surface laser spallation) at a depth(s) where the tensile component of the wave exceeds the dynamics strength of the (typically melted) material; (c) interaction of the pressure wave with the back surface of the target leading to back spallation, disintegration of the layer ejected from the front surface into clusters/droplets.

electrons before the electron-phonon equilibration, L_c, define the condition for the stress confinement, $max\{\tau_p, \tau_{e\text{-}ph}\} \leq \tau_s \sim L_c/C_s$ [10].

The processes of photomechanical front- and back-surface spallation are schematically illustrated in Figure 6. Short pulse laser irradiation occurring under conditions of stress confinement results in the generation of high compressive stresses in the surface region of the target (Figure 6a). The interaction of the initial compressive stresses with the free surface of the target results in the development of a tensile component of the pressure wave that propagates deeper into the bulk of the target. The tensile stresses are increasing with depth and can overcome the dynamic strength of the target material, leading to the mechanical separation and ejection of a front layer of the target (Figure 6b). At later times the layer ejected from the front surface can disintegrate into clusters/droplets, whereas the pressure wave can reach the back surface of the target and cause back-surface spallation (Figure 6c).

The microscopic mechanisms of front-surface spallation has been investigated in a number of recent MD simulations performed for molecular systems [10,35,36,36,37,38] and metal targets [8,10]. Nucleation, growth and coalescence of voids have been identified as the main processes responsible for laser spallation in both systems. In particular, two stages have been identified in the evolution of voids in laser spallation of molecular targets, the initial void nucleation and growth, when the number of voids of all sizes is increasing with time and (2) void coarsening and coalescence, when the number of large voids increases at the expense of quickly decreasing population of small voids [10]. Below we perform an analysis of the evolution of photomechanical damage in a large-scale MD simulation of laser spallation of a 100 nm Ni film irradiated by a picosecond laser pulse. Simulation results are related to earlier observations obtained for laser spallation of molecular and metal targets.

4.1. Laser spallation of 100 nm Ni film: two stages of void evolution

The temperature and pressure contour plots for a simulation performed for 100 nm film at a laser fluence of 1623 J/m^2 are shown in Figure 7. Laser excitation of free electrons and fast energy transfer to the lattice vibrations leads to the initial temperature increase in the area adjacent to the irradiated surface of the film, Figure 7a. The temperature increase, occurring under conditions of stress confinement [10] leads to the compressive pressure buildup which, in turn, relaxes by driving a compressive pressure wave toward the back surface of the film (solid white arrow in Figure 7b). The relaxation of the initial compressive pressure near the free surface leads to the development of an unloading tensile component of the pressure wave that follows the compressive component (dashed white arrow in Figure 7b). The compressive pressure wave transforms into a tensile one upon reflection from the back surface of the film (another dashed arrow in Figure 7b). The two tensile waves superimpose with each other, generating the maximum tensile stresses in a region located at a depth of around -25 nm at a time of ~35 ps.

Further evolution of the pressure waves in the film is strongly affected by the onset of photomechanical damage that is clearly visible in the density contour plot shown in Figure 7c and in the snapshots from the simulation shown in Figures 8 and 9. An active growth of voids starts at depths from 10 nm to 40 nm at ~32 ps (Figures 7c and 9). This time of the onset of void nucleation coincides with the passage of the tensile pressure wave, Figure 7b. The area affected by photomechanical damage quickly expands and voids can be seen at the depths from -30 nm to 50 nm by the time of 40 ps (Figures 7c, 8 and 9). Note that the region of the active void evolution is shifted toward the irradiated front surface of the film with respect to the depth where the maximum tensile stresses are created. The voids appear and grow at depths defined by the competition between the tensile stresses that are increasing with depth and the decreasing thermal softening of the target material [10,35,36].

Similarly to the laser spallation of molecular targets reported earlier [10,37], two stages of the evolution of photomechanical damage can be identified. The initial stage of void nucleation and growth is characterized by the increase of both the number of voids and the range of void sizes, as can be seen from Figure 10a, where the void volume distributions are shown for 30 ps and 34 ps after the laser pulse. After ~34 ps, the second stage of void coarsening and coalescence can be identified, when the number of small voids is decreasing and large voids appear as a result of coalescence of smaller voids, Figure 10b. The second stage of the void evolution leads to the eventual percolation of the empty volume and disintegration of the film.

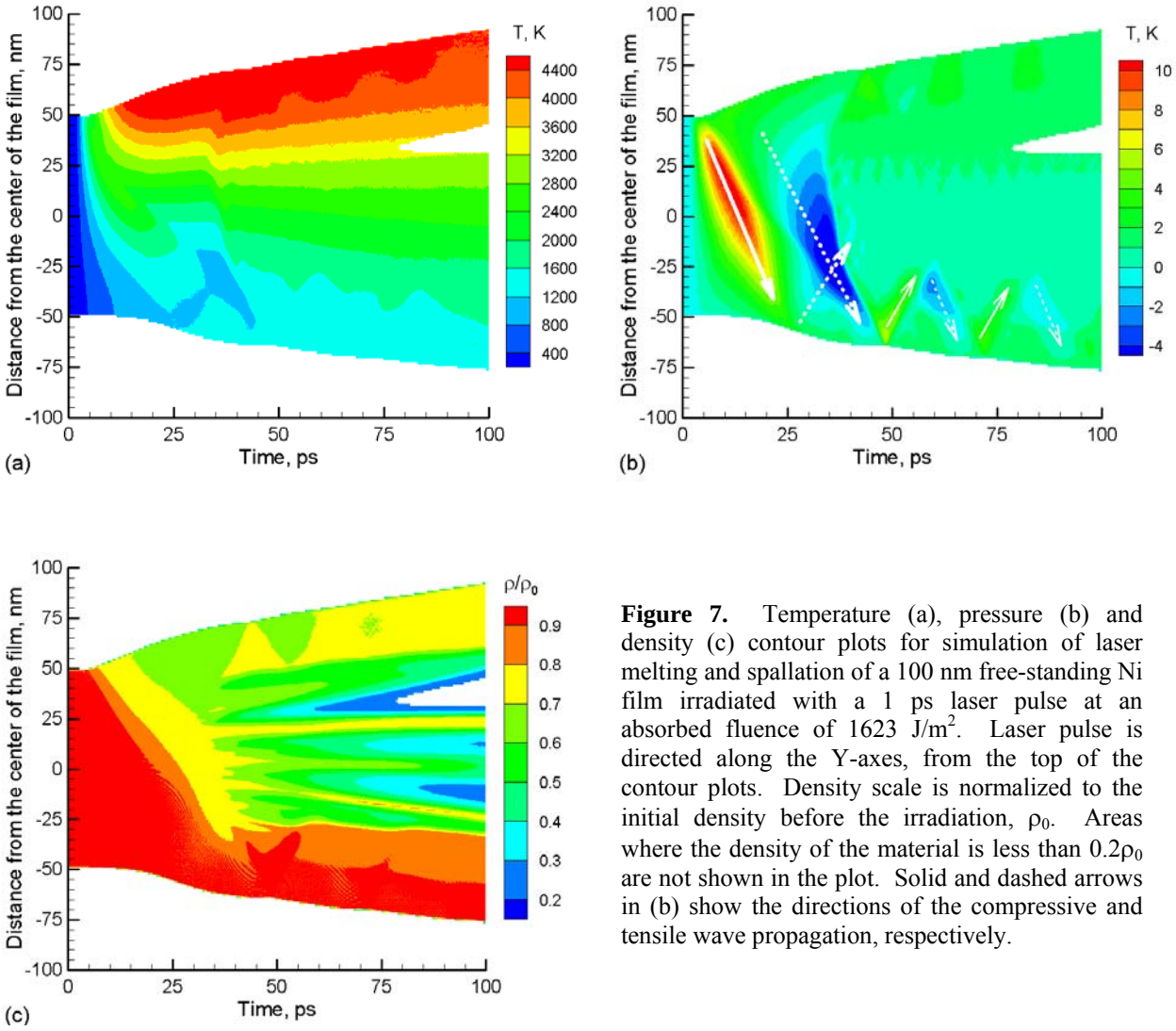

Figure 7. Temperature (a), pressure (b) and density (c) contour plots for simulation of laser melting and spallation of a 100 nm free-standing Ni film irradiated with a 1 ps laser pulse at an absorbed fluence of 1623 J/m^2. Laser pulse is directed along the Y-axes, from the top of the contour plots. Density scale is normalized to the initial density before the irradiation, ρ_0. Areas where the density of the material is less than $0.2\rho_0$ are not shown in the plot. Solid and dashed arrows in (b) show the directions of the compressive and tensile wave propagation, respectively.

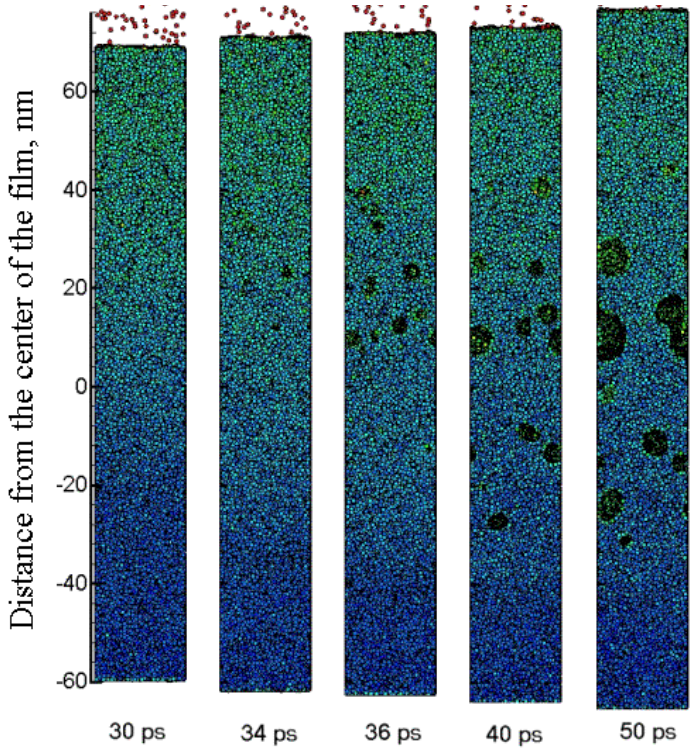

Figure 8. Snapshots from simulation of a 100 nm Ni film irradiated with 1 ps laser pulse at an absorbed fluence of 1623 J/m^2. Atoms are colored according to their potential energy (red color corresponds to high potential energy of -0.7 eV, blue color corresponds to low energy of -4.5 eV, the cohesive energy of the EAM Ni fcc crystal is 4.45 eV).

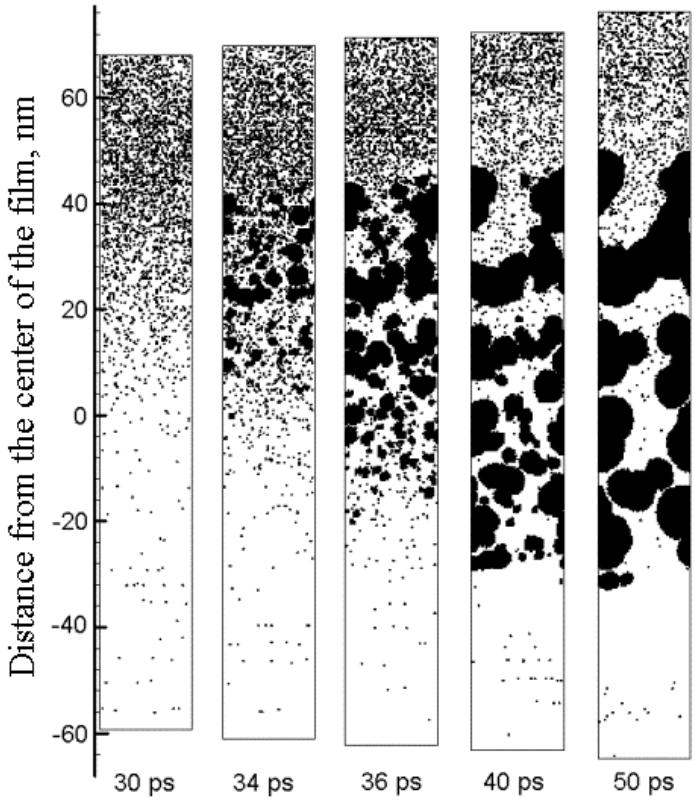

Figure 9. Representation of the evolution of voids (empty space) in the same simulation for which atomic configurations are shown in Figure 8. The voids are defined by superimposing atomic configurations with a three-dimensional grid of cubic cells with a size of 0.33 nm and identifying cells that do not contain any atoms. Voids are defined as clusters of more than two empty cells connected with each other by sharing a face.

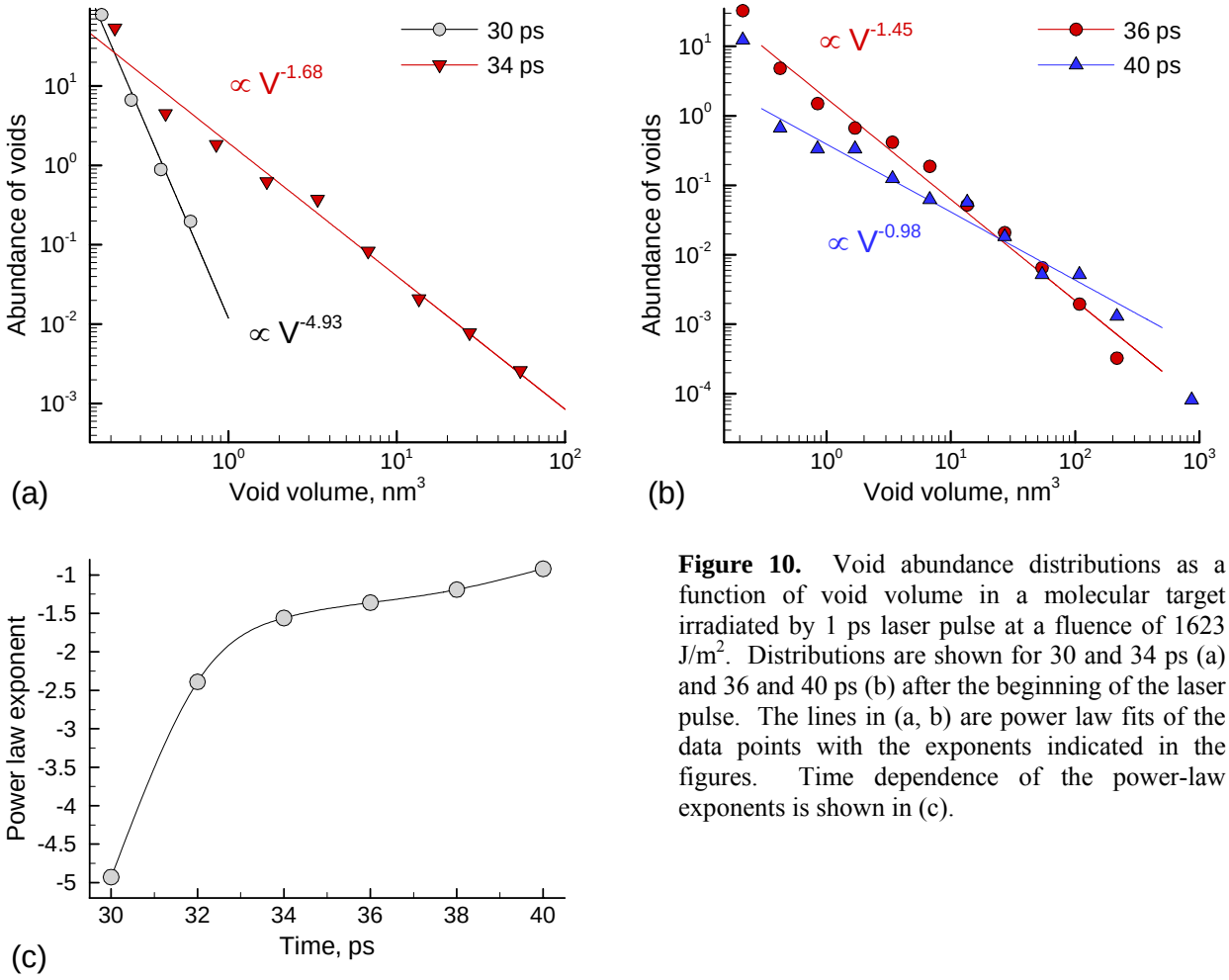

Figure 10. Void abundance distributions as a function of void volume in a molecular target irradiated by 1 ps laser pulse at a fluence of 1623 J/m^2. Distributions are shown for 30 and 34 ps (a) and 36 and 40 ps (b) after the beginning of the laser pulse. The lines in (a, b) are power law fits of the data points with the exponents indicated in the figures. Time dependence of the power-law exponents is shown in (c).

In both regimes the size distributions of voids can be relatively well described by a power law $N(V) \sim V^{-\tau}$ with an exponent $-\tau$ gradually increasing with time, Figure 10c. The observed changes of the power law exponent during the evolution of photomechanical damage are in a very good quantitative agreement with the ones observed for laser spallation of molecular targets [10,37]. Moreover, power law dependences have been predicted for the cluster size distributions in a recent computational study of laser ablation [39] as well as for void volume distributions observed in MD simulations of shock-induced back spallation in metal targets [40]. The critical power law exponent observed for void distribution in MD simulations of shock-induced back spallation, $\tau \sim 2.2$ [40], is close to the ones that separate the two regimes of void evolution observed in the simulations of laser-induced spallation of two drastically different materials, amorphous molecular systems and crystalline metal targets. These observations suggest that the spallation mechanisms described above may reflect general characteristics of the dynamic fracture at high deformation rates.

ACKNOWLEDGEMENTS

Financial support of this work is provided by the National Science Foundation through the Thermal Transport and Thermal Processes Program of the Chemical and Transport Systems Division.

REFERENCES

[1] B. J. Siwick, J. R. Dwyer, R. E. Jordan, and R. J. D. Miller, An atomic-level view of melting using femtosecond electron diffraction, *Science* **302**, 1382-1385, 2003.

[2] K. Sokolowski-Tinten, C. Blome, J. Blums, A. Cavalleri, C. Dietrich, A. Tarasevich, I. Uschmann, E. Forster, M. Kammler, M. Horn-von-Hoegen, and D. von der Linde, Femtosecond X-ray measurement of coherent lattice vibrations near the Lindemann stability limit, *Nature* **422**, 287-289, 2003.

[3] M. B. Agranat, S. I. Ashitkov, V. E. Fortov, A. V. Kirillin, A. V. Kostanovskii, S. I. Anisimov, P. S. Kondratenko, Use of optical anisotropy for study of ultrafast phase transformations at solid surfaces, *Appl. Phys. A* **69**, 637-640, 1999.

[4] B. Lin and H. E. Elsayed–Ali, Temperature dependent reflection electron diffraction study of In(111) and observation of laser-induced transient surface superheating, *Surf. Sci.* **498**, 275-284, 2002.

[5] J. Hohlfeld, S.-S. Wellershoff, J. Gudde, U. Conrad, V. Jahnke, and E. Matthias, Electron and lattice dynamics following optical excitation of metals, *Chem. Phys.* **251**, 237-258, 2000.

[6] K. Sokolowski-Tinten, J. Bialkowski, M. Boing, A. Cavalleri, and D. von der Linde, Thermal and nontermal melting of gallium arsenide after femtosecond laser excitation, *Phys. Rev. B* **58**, R11805-R11808, 1998.

[7] D. S. Ivanov and L. V. Zhigilei, The effect of pressure relaxation on the mechanisms of short pulse laser melting, *Phys. Rev. Lett.* **91**, 105701, 2003.

[8] D. S. Ivanov and L. V. Zhigilei, Combined atomistic-continuum modeling of short pulse laser melting and disintegration of metal films, *Phys. Rev. B* **68**, 064114, 2003.

[9] D. S. Ivanov and L. V. Zhigilei, Combined atomistic - continuum model for simulation of laser interaction with metals: application to calculation of melting thresholds in Ni targets of varying thickness, *Appl. Phys. A*, in press.

[10] E. Leveugle, D. S. Ivanov, and L. V. Zhigilei, Photomechanical spallation of molecular and metal targets: molecular dynamics study, *Appl. Phys. A*, in press.

[11] C. Schafer, H. M. Urbassek, and L. V. Zhigilei, Metal ablation by picosecond laser pulses: A hybrid simulation, *Phys. Rev. B* **66**, 115404, 2002.

[12] D. S. Ivanov, L. V. Zhigilei, E. M. Bringa, M. De Koning, B. A. Remington, M. J. Caturla, and S. M. Pollaine, Molecular dynamics simulations of shocks including electronic heat conduction and electron-phonon coupling, *Proceedings of 2003 APS Topical Conference on Shock Compression of Condensed Matter*, in press.

[13] E. Ohmura and I. Fukumoto, Modified molecular dynamics simulation on laser ablation of metal, *Int. J. Japan Soc. Prec. Eng.* **31**, 206-207, 1997.

[14] M. I. Kaganov, I. M. Lifshitz, and L. V. Tanatarov, Relaxation between electrons and crystalline lattices, *Sov. Phys. JETP* **4**, 173-178, 1957.

[15] S. I. Anisimov, B. L. Kapeliovich, and T. L. Perel'man, Electron emission from metal surfaces exposed to ultrashort laser pulses, *Sov. Phys. JETP* **39**, 375-377, 1974.

[16] G. L. Eesley, Generation of nonequilibrium electron and lattice temperatures in copper by picosecond laser pulses, *Phys. Rev. B* **33**, 2144-2151, 1986.

[17] H. E. Elsayed-Ali, T. Juhasz, G. O. Smith, and W. E. Bron, Femtosecond thermoreflectivity and thermotransmissivity of polycrystalline and single-crystalline gold films, *Phys. Rev. B* **43**, 4488-4491, 1991.

[18] P. M. Norris, A. P. Caffrey, R. J. Stevens, J. M. Klopf, J. T. McLeskey, Jr., and A. N. Smith, Femtosecond pump-probe nondestructive evaluation of materials, *Rev. Sci. Instrum.* **74**, 400-406, 2003.

[19] P. J. Antaki, Importance of nonequilibrium thermal conductivity during short-pulse laser-induced desorption from metals, *Int. J. Heat Mass Tran.* **45**, 4063-4067, 2002.

[20] V. Schmidt, W. Husinsky, G. Betz, Ultrashort laser ablation of metals: pump-probe experiments, the role of ballistic electrons and the two-temperature model, *Appl. Surf. Sci.* **197**, 145-155, 2002.

[21] J. K. Chen and J. E. Beraun, Modeling of ultrafast laser ablation of gold films in vacuum, *J. Opt. A,* **5**, 168-173, 2003.

[22] J. K. Chen, J. E. Beraun, L. E. Grimes, and D. Y. Tzou, Modeling of femtosecond laser-induced non-equilibrium deformation in metal films, *Int. J. Solids Struct.* **39**, 3199-3216, 2002.

[23] L. V. Zhigilei and B. J. Garrison, Pressure waves in microscopic simulations of laser ablation, *Mat. Res. Soc. Symp. Proc.* **538**, 491-496, 1999.

[24] C. Schafer, H. M. Urbassek, L. V. Zhigilei, and B. J. Garrison, Pressure-transmitting boundary conditions for molecular dynamics simulations, *Comp. Mater. Sci.* **24**, 421-429, 2002.

[25] M. S. Daw, S. M. Foiles, and M. I. Baskes, The embedded-atom method: a review of theory and applications, *Mat. Sci. Rep*. **9**, 251-310, 1993.

[26] X. W. Zhou, H. N. G. Wadley, R. A. Johnson, D. J. Larson, N. Tabat, A. Cerezo, A. K. Petford-Long, G. D. W. Smith, P. H. Clifton, R. L. Martens, and T. F. Kelly, Atomic scale structure of sputtered metal multilayers, *Acta Mater*. **49**, 4005-4015, 2001.

[27] *American Institute of Physics Handbook* (New-York: McGraw-Hill, 3rd ed., 1972).

[28] Y. S. Touloukian, *Thermophysical Properties of Matter*, *Vol. 12: Thermal expansion: metallic elements and alloys* (New York: IFI/Plenum, 1975).

[29] F. Spaepen and D. Turnbull, Kinetics of motion of crystal-melt interfaces, in *Laser Solid Interactions and Laser Processing*, AIP Conference Proceedings, 1979, pp. 50-73.

[30] V. I. Motorin and S. L. Musher, Stability and liquefaction front in fast Joule heating, *Sov. Phys. - Tech. Phys.* **27**, 726-729, 1982.

[31] B. Rethfeld, K. Sokolowski-Tinten, D. von der Linde, and S. I. Anisimov, Ultrafast thermal melting of laser-excited solids by homogeneous nucleation, *Phys. Rev. B* **65**, 092103, 2002.

[32] K. Lu and Y. Li, Homogeneous nucleation catastrophe as a kinetic stability limit for superheated crystal, *Phys. Rev. Lett.* **80**, 4474-4477, 1998.

[33] Animated sequences of snapshots from a molecular dynamics simulation of laser melting can be found at http://www.faculty.virginia.edu/CompMat/melting/animations/

[34] G. Paltauf and P. E. Dyer, Photomechanical processes and effects in ablation, *Chem. Rev.* **103**, 487-518, 2003.

[35] L. V. Zhigilei and B. J. Garrison, Microscopic mechanisms of laser ablation of organic solids in the thermal and stress confinement irradiation regimes, *J. Appl. Phys.* **88**, 1281-1298, 2000.

[36] L. V. Zhigilei, E. Leveugle, B. J. Garrison, Y. G. Yingling, and M. I. Zeifman, Computer simulations of laser ablation of molecular substrates, *Chem. Rev.* **103**, 321-348, 2003.

[37] E. Leveugle and L. V. Zhigilei, Microscopic mechanisms of short pulse laser spallation of molecular solids, *Appl. Phys. A*, in press.

[38] Animated sequences of snapshots from a molecular dynamics simulation of laser spallation of a molecular target can be found at http://www.faculty.virginia.edu/CompMat/spallation/animations/

[39] L. V. Zhigilei, Dynamics of the plume formation and parameters of the ejected clusters in short-pulse laser ablation, *Appl. Phys. A* **76**, 339-350, 2003.

[40] A. Strachan, T. Cagin, and W. A. Goddard III, Critical behavior in spallation failure of metals, *Phys. Rev. B* **63**, 060103, 2001.